

Evaluating radiation transport errors in merger simulations using a Monte Carlo algorithm

F. Foucart,¹ M. D. Duez,² L. E. Kidder,³ R. Nguyen,¹ H. P. Pfeiffer,^{4,5} and M. A. Scheel⁶

¹*Department of Physics, University of New Hampshire, 9 Library Way, Durham, New Hampshire 03824, USA*

²*Department of Physics & Astronomy, Washington State University, Pullman, Washington 99164, USA*

³*Cornell Center for Astrophysics and Planetary Science, Cornell University, Ithaca, New York 14853, USA*

⁴*Max Planck Institute for Gravitational Physics (Albert Einstein Institute), D-14476 Potsdam-Golm, Germany*

⁵*Canadian Institute for Theoretical Astrophysics, University of Toronto, Toronto, Ontario M5S 3H8, Canada*

⁶*TAPIR, Walter Burke Institute for Theoretical Physics, MC 350-17, California Institute of Technology, Pasadena, California 91125, USA*



(Received 8 June 2018; published 11 September 2018)

Neutrino-matter interactions play an important role in the postmerger evolution of neutron star-neutron star and black hole-neutron star mergers. Most notably, they determine the properties of the bright optical/infrared transients observable after a merger. Unfortunately, Boltzmann's equations of radiation transport remain too costly to be evolved directly in merger simulations. Simulations rely instead on approximate transport algorithms with unquantified modeling errors. In this paper, we use for the first time a time-dependent general relativistic Monte Carlo (MC) algorithm to solve Boltzmann's equations and estimate important properties of the neutrino distribution function ~ 10 ms after a neutron star merger that resulted in the formation of a massive neutron star surrounded by an accretion disk. We do not fully couple the MC algorithm to the fluid evolution, but use a short evolution of the merger remnant to critically assess errors in our approximate gray two-moment transport scheme. We demonstrate that the analytical closure used by the moment scheme is highly inaccurate in the polar regions, but performs well elsewhere. While the average energy of polar neutrinos is reasonably well captured by the two-moment scheme, estimates for the neutrino energy become less accurate at lower latitudes. The two-moment formalism also overestimates the density of neutrinos in the polar regions by $\sim 50\%$, and underestimates the neutrino pair-annihilation rate at the poles by factors of 2–3. Although the latter is significantly more accurate than one might have expected before this study, our results indicate that predictions for the properties of polar outflows and for the creation of a baryon-free region at the poles are likely to be affected by errors in the two-moment scheme, thus limiting our ability to reliably model kilonovae and gamma-ray bursts.

DOI: [10.1103/PhysRevD.98.063007](https://doi.org/10.1103/PhysRevD.98.063007)

I. INTRODUCTION

The recent detection by the LIGO-Virgo Collaboration of gravitational waves (GWs) powered by a pair of merging neutron stars (GW170817 [1]), followed by electromagnetic (EM) observations of the same system by a wide range of ground-based and space-based telescopes [2], represents a major breakthrough for multimessenger astronomy. This event also shows the current limits of our ability to reliably extract information about merging compact objects using EM observations. For example, GW170817 was followed by a bright *kilonova* [3–15], an optical/infrared transient powered by radioactive decays in the neutron-rich ejecta produced by the merger [16–20]. EM observations of that kilonova have been used to infer plausible properties of the ejecta, and the outcome of r-process nucleosynthesis in

the outflows. Determining the properties of the merging objects from those of the ejecta, however, remains difficult.

To better constrain the properties of the merging objects from kilonova observations, we require numerical simulations of neutron star mergers capable of accurately predicting the properties of the ejected material. Unfortunately, despite rapid improvements in the accuracy and physical realism of these simulations, a few important issues are still limiting our ability to make such predictions.

A first problem is that outflows are produced both during the merger (dynamical ejecta), and over the much slower evolution of the postmerger accretion disk (disk outflows), thus requiring simulations covering a wide range of time-scales and length scales. Only a few simulations so far have attempted to self-consistently include both phases of the evolution [21–23].

Another issue is that magnetic fields play a critical role in driving disk outflows, and in the postmerger evolution of the system [24–26]. Yet these fields grow from very small scale instabilities that current simulations do not properly resolve [24]. So far, these effects have only been approximately captured through the use of subgrid models [27–29], or of unphysically large initial magnetic fields (see e.g., [30,31] for reviews of the field).

Finally, neutrino-matter interactions play a critical role in the evolution of the composition of the outflows [32,33], are the main source of cooling in the postmerger remnant, can drive disk winds [22,34], and deposit a large amount of energy in the polar regions through pair annihilation [35–40]. As Boltzmann’s equations of radiation transport remain too costly to include in 3D simulations, however, we rely on approximate transport methods to estimate the impact of neutrino-matter interactions in merger remnants.

Here, we focus on the latter issue. In particular, we note that approximate transport algorithms currently used in merger simulations come with potentially significant and, more importantly, so far unquantified errors. To work towards a more rigorous determination of error budgets in simulations, we use our recently developed general relativistic MC radiation transport code [41] to evolve over a small time interval the remnant of a binary neutron star merger. We do not fully couple the MC evolution to the fluid evolution: neutrino-matter interactions are still handled using our approximate, gray two-moment scheme [42–44] with Minerbo closure [45]. Instead, we use the MC evolution to obtain more accurate estimates of the neutrino distribution function. This allows us to constrain the accuracy of simulations that use approximate two-moment transport schemes. Such error estimates are critical to our ability to assess the robustness of kilonova models, as simulations using the two-moment scheme are being used to model merger outflows and to interpret kilonova observations.

This MC simulation also provides us with an opportunity to study more carefully the properties of neutrinos emitted by the remnant of neutron star mergers. For the first time, we have at our disposal an estimate of the 7-dimensional neutrino distribution function, $f_{(\nu_i)}(t, x^i, p_i)$ (with t the time, x^i the spatial coordinates, and p_i the spatial components of the 4-momentum of the neutrinos) for each neutrino species ν_i , obtained from a time-dependent evolution of Boltzmann’s equations, in general relativity and with a realistic background for the metric and fluid properties. Knowing $f_{(\nu_i)}$, rather than its lowest moments in momentum space, is important for accurate estimates of the rate of $\nu\bar{\nu}$ annihilations [35,38], and for studies of more complex neutrino processes currently not included in merger simulations (e.g., neutrino oscillations [46–49]). We illustrate this advantage of the MC scheme by providing the energy spectrum of neutrinos, their angular distribution at selected points in the simulation, and the heating rate of the fluid due to $\nu\bar{\nu}$ annihilation in the polar regions.

II. METHODS

A. Evolution algorithm

In this work, we evolve the remnant of a binary neutron star merger with our general relativistic radiation hydrodynamics code, SpEC [50]. SpEC evolves Einstein’s equations of general relativity on a pseudospectral grid, using the generalized harmonic formalism [51]. The general relativistic equations of hydrodynamics are evolved on a separate numerical grid using high-order shock capturing finite volume methods [52]. A more detailed description of our latest methods to evolve the metric and fluid in SpEC can be found in [53].

We also evolve the general relativistic equations of neutrino radiation transport using a gray (i.e., energy-integrated) two-moment formalism [54,55]. We only use 3 distinct species of neutrinos: electron neutrinos ν_e , electron antineutrinos $\bar{\nu}_e$, and heavy-lepton neutrinos ν_x . The latter class includes muon and tau (anti)neutrinos, $(\nu_\mu, \bar{\nu}_\mu, \nu_\tau, \bar{\nu}_\tau)$. At the densities and temperatures encountered in neutron star mergers, the fraction of heavy leptons (μ, τ) in the fluid is much smaller than the fraction of electrons/positrons, and we thus make the assumption that the 4 species gathered in ν_x are largely interchangeable.¹ A detailed description of our implementation of the moment formalism is provided in [43,44]. Here, we limit ourselves to a discussion of the most important aspects of the algorithm for the purpose of estimating errors in the two-moment formalism.

In the moment formalism, we evolve the lowest moments of the neutrino distribution function $f_{(\nu_i)}(t, x^i, p_i)$ in momentum space. In a coordinate system comoving with the fluid, the 0th, 1st, and 2nd moments are the energy density J , momentum density H^μ , and pressure tensor $S^{\mu\nu}$. These moments can be explicitly written as the momentum-space integrals

$$J_{(\nu_i)} = \int d\nu \nu^3 \int d\Omega f_{(\nu_i)}, \quad (1)$$

$$H_{(\nu_i)}^\mu = \int d\nu \nu^3 \int d\Omega f_{(\nu_i)} l^\mu, \quad (2)$$

$$S_{(\nu_i)}^{\mu\nu} = \int d\nu \nu^3 \int d\Omega f_{(\nu_i)} l^\mu l^\nu, \quad (3)$$

with ν the neutrino energy in the fluid frame, $\int d\Omega$ an integral over the solid angle on a unit sphere in momentum space, and

$$p^\mu = \nu(u^\mu + l^\mu) \quad (4)$$

¹Muon production may, however, impact the equation of state of neutron star matter, and indirectly affect the properties of the emitted neutrinos [56].

the 4-momentum of neutrinos, with u^μ the 4-velocity of the fluid and $l^\mu u_\mu = 0$. The stress-energy tensor of the neutrinos is then, for species ν_i ,

$$T_{(\nu_i)}^{\mu\nu} = J_{(\nu_i)} u^\mu u^\nu + H_{(\nu_i)}^\mu u^\nu + H_{(\nu_i)}^\nu u^\mu + S_{(\nu_i)}^{\mu\nu}. \quad (5)$$

In simulations, we also define the energy density $E_{(\nu_i)}$, momentum density $F_{(\nu_i),\mu}$, and pressure tensor $P_{(\nu_i),\mu\nu}$ measured by an observer whose worldline is tangent to n^μ , the unit normal to a $t = \text{constant}$ hypersurface (inertial observer). The stress-energy tensor is then

$$T_{(\nu_i)}^{\mu\nu} = E_{(\nu_i)} n^\mu n^\nu + F_{(\nu_i)}^\mu n^\nu + F_{(\nu_i)}^\nu n^\mu + P_{(\nu_i)}^{\mu\nu}, \quad (6)$$

with $F_{(\nu_i)}^\mu n_\mu = P_{(\nu_i)}^{\mu\nu} n_\mu = P_{(\nu_i)}^{\mu\nu} n_\nu = 0$. For convenience, in the rest of this paper we drop the subscript (ν_i) when referring to moments of $f_{(\nu_i)}$, but moments should always be understood as referring to a specific neutrino species. The moment formalism provides us with evolution equations for E and F_i , the spatial components of F_μ . They can be expressed in the familiar form

$$\nabla_\mu T_{(\nu_i)}^{\mu\nu} = Q_{(\nu_i)}^\nu \quad (7)$$

for some source terms $Q_{(\nu_i)}^\nu$ capturing interactions between neutrinos of species (ν_i) and the fluid, as well as interactions with other neutrino species. We also evolve the number density of neutrinos as measured by an inertial observer, N (see [44]). This allows us to locally compute the average energy of the neutrinos as measured by an inertial observer,

$$\langle \epsilon \rangle = \frac{E}{N}. \quad (8)$$

We note that, unless specified otherwise, average energy in this paper refers to the number-density weighted average of the neutrino energy, in a frame to be specified. Finally, the evolution of the fluid is given by the equations

$$\nabla_\mu T_{\text{fl}}^{\mu\nu} = -\sum_{(\nu_i)} Q_{(\nu_i)}^\nu, \quad (9)$$

$$\nabla_\mu (\rho \sqrt{-g} u^\mu) = 0, \quad (10)$$

with $T_{\text{fl}}^{\mu\nu}$ the stress-energy tensor of the fluid, ρ the baryon density, and g the determinant of the 4-metric.

Equation (7) is exact, but depends on the unknown pressure tensor of the neutrinos, P_{ij} . In SpEC, we close the system of equations using the Minerbo closure [45]. Effectively, P_{ij} is estimated by interpolating between its analytically known value in optically thick regions (isotropic pressure in thermal equilibrium with the fluid) and its value for a single beam of neutrinos propagating in

vacuum. This is expected to be very accurate in regions of high optical depth, qualitatively correct in semitransparent regions, and completely wrong in optically thin regions if neutrinos come from more than one direction. Once we have chosen a closure $P_{ij}(E, F_i)$, Eq. (7) is a system of 4 equations for the 4 unknown (E, F_i) , for each neutrino species.

Besides a choice of closure, the gray two-moment scheme relies on significant approximations in the computation of $Q_{(\nu_i)}^\nu$. We include in $Q_{(\nu_i)}^\nu$ charged-current reactions

$$p + e^- \leftrightarrow n + \nu_e \quad (11)$$

$$n + e^+ \leftrightarrow p + \bar{\nu}_e, \quad (12)$$

$\nu\bar{\nu}$ pair annihilation/creation

$$e^+ + e^- \leftrightarrow \nu + \bar{\nu}, \quad (13)$$

plasmon decays

$$\gamma \leftrightarrow \nu + \bar{\nu}, \quad (14)$$

and, for heavy-lepton neutrinos, nucleon-nucleon Bremsstrahlung (note that $\bar{\nu}_x = \nu_x$ in SpEC)

$$N + N \leftrightarrow N + N + \nu_x + \bar{\nu}_x. \quad (15)$$

All of the emissivities and absorption opacities are computed following [57], except for nucleon-nucleon Bremsstrahlung [58]. We compute the neutrino absorption opacities $\kappa_{a,(\nu_i)}$ due to charged-current reactions and the neutrino emissivities $\eta_{(\nu_i)}$ due to other processes. The emissivities due to charged-current reactions and absorption opacities due to other processes are computed by imposing Kirchoff's law, $\eta = B\kappa_a$, with B the energy density of neutrinos in equilibrium with the fluid. Using Kirchoff's law guarantees that we recover the correct neutrino energy density in optically thick regions. We also compute the scattering opacities $\kappa_{s,(\nu_i)}$ due to elastic scattering of neutrinos on neutrons, protons, and heavy nuclei [57], and estimate

$$Q_{(\nu_i)}^\nu = \eta_{(\nu_i)} u^\nu - \kappa_{a,(\nu_i)} J u^\nu - (\kappa_{a,(\nu_i)} + \kappa_{s,(\nu_i)}) H^\nu. \quad (16)$$

We ignore inelastic scatterings, as well as all processes not explicitly mentioned here.

An important issue when computing $Q_{(\nu_i)}^\nu$ is that the cross sections for the above reactions depend on the energy spectrum of the neutrinos. In a gray scheme, we can only guess what that spectrum is. To compute opacities, we thus first assume that the neutrinos are in thermal equilibrium with the fluid. We then compute the average energy of the neutrinos from their moments (E, F_i, N) , and rely on a fairly complex and somewhat arbitrary procedure to

estimate the shape of the neutrino spectrum in optically thin regions. We then correct the absorption and scattering opacities, assuming a ν^2 dependence for the dominant neutrino-matter interactions (see [44]).

The situation is even worse in simulations that do not evolve the number density N . Then, even finding a good estimate of the average energy of neutrinos can be difficult. For neutron star mergers, this leads to large errors in the absorption rate of neutrinos in optically thin regions as well as in the composition of polar outflows [44].

Another problem with the two-moment scheme is that the rate of $\nu\bar{\nu}$ pair annihilation in optically thin regions is highly dependent on the momentum distribution of neutrinos, as the pair annihilation cross section grows rapidly with the angle between the direction of propagation of the neutrino and the antineutrino. The pair annihilation rate is also very poorly approximated by Kirchoff's law in regions where the number density of electrons or positrons is low. We discuss below an approximate treatment of these annihilation processes, proposed by Fujibayashi *et al.* [38]. Within the framework of a gray two-moment scheme, however, any estimate of $\nu\bar{\nu}$ pair annihilation has potentially large errors.

To quantify these errors in the two-moment scheme, we rely on a newly developed MC scheme, described in detail in [41]. The MC algorithm implemented in SpEC is largely inspired by earlier work on MC evolution of neutrinos in special relativity [59] and on general relativistic photon transport [60]. In particular, we evolve *packets* of neutrinos, each representing N_k neutrinos of 4-momentum p_k^μ at position x_k^i . The MC representation of the neutrino distribution function is then

$$f_{(\nu),MC} = \sum_k N_k \delta^3(x^i - x_k^i) \delta^3(p_i - p_k^i) \quad (17)$$

while the stress-energy tensor of the neutrinos can be estimated as [60]

$$T_{\mu\nu,MC} = \sum_k N_k \frac{p_k^\mu p_k^\nu}{\sqrt{\gamma} \alpha p_k^t} \delta^3(x^i - x_k^i). \quad (18)$$

In practice, we can estimate these functions by replacing $\delta^3(x^i - x_k^i)$ by a function $f(x^i)$ of unit norm (and, for $f_{(\nu)}$, by binning in momentum space). This is the procedure that we follow in this paper, with either $f(x^i) = V^{-1}$ within a volume V , or $f(x^i)$ a normalized Gaussian of width σ . The stress-energy tensor can also be time-averaged to allow for the accumulation of more packets, as proposed in [41].

The MC scheme can theoretically be used as a closure for the two-moment algorithm. Doing this leads to a scheme that evolves Boltzmann's equations to numerical accuracy. For this first use in merger simulations, however, we consider a simpler, cheaper, and possibly more stable

setup (the stability of the coupled M1-MC system has not been demonstrated). We evolve the equations of radiation-hydrodynamics using the two-moment scheme with Minerbo closure (we refer to this as the M1 scheme in the rest of this paper). The resulting time-dependent fluid quantities are used as background for the MC evolution. The MC evolution does not feed back onto either the fluid or the two-moment evolution. Each MC packet is created with a fluid frame energy of $10^{-11} M_\odot c^2$.

The MC algorithm implemented in SpEC is currently capable of handling isotropic emission of neutrinos in the fluid frame, transport of neutrinos along geodesics, neutrino absorption, and elastic scattering. We use the publicly available NuLib library [61] to generate a table of neutrino emissivities and absorption/scattering opacities as a function of fluid-frame neutrino energy ν , fluid density ρ , fluid temperature T , and fluid electron fraction Y_e . The table has 12 energy bins spanning $\nu \in [0, 150]$ MeV, with a logarithmic spacing between bins (except that the first 2 bins have a width of 4 MeV). We also use 51 equally spaced bins for $Y_e \in [0.035, 0.55]$, 82 logarithmically spaced bins for $\rho \in [10^6, 3.16 \times 10^{15}]$ g/cm³, and 65 logarithmically spaced bins for $T \in [0.05, 150]$ MeV. In between tabulated points, we interpolate the logarithm of the energy-dependent opacities (κ_a, κ_s) linearly in Y_e and logarithmically in the other variables. Following Richers *et al.* [59], we always emit particles with a fluid-frame energy at the center of an energy bin. The NuLib table uses the same set of reactions as the moment scheme, except that it neglects all pair processes for $\nu_e \bar{\nu}_e$. The effective gray opacities derived from the MC evolution could, however, be very different from those in the moment scheme, as the MC algorithm is fully energy dependent while the moment scheme arbitrarily assumes a given neutrino spectrum at each point.

An important property of our MC algorithm is that it ignores regions of high optical depth, where the two-moment scheme is reliable and the neutrino distribution function is well approximated by a thermal distribution in equilibrium with the fluid. The MC algorithm only evolves regions of the postmerger remnant where $\kappa_a(\kappa_a + \kappa_s) \lesssim \kappa_{\text{crit}}^2$. In any cell that does not satisfy this condition, but with a neighboring cell that does, MC particles are erased at the end of each time step and redrawn from an equilibrium distribution. This provides a boundary condition for our MC algorithm. We note that we evaluate opacities separately for each energy bin, and that "neighbors" are determined in a 4D space (3 spatial dimensions, plus ν).

We choose κ_{crit} so that in any region where the characteristic length scale for variation of the opacities is at least a few grid cells, the assumption of an equilibrium distribution of neutrinos in these "high-opacity" cells is reasonably accurate. For example, for an optically thick sphere of constant opacity κ_0 , the relative difference between the energy density of neutrinos and the equilibrium density of neutrinos at distances Δx from the surface is $\sim (0.08, 0.02, 0.005)$ for

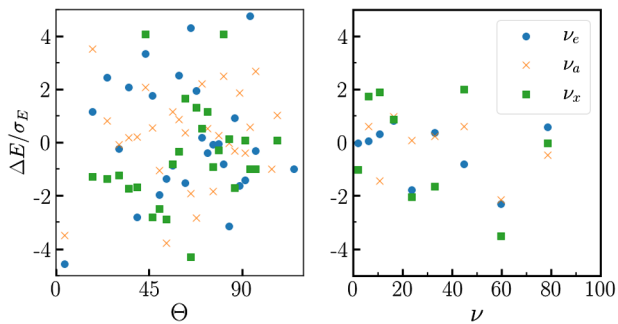


FIG. 1. Difference in the pitch-angle distribution and energy spectrum of neutrinos between two simulations placing the boundary of the MC evolution at different optical depth. We look at neutrinos within a 3 km radius of a point on the polar axis ($z = 45$ km), about 5 ms after the beginning of the simulation. Errors are normalized by the expected Poisson error in our reference simulation. Both simulations have near-identical Poisson noise.

optical depth $\tau = \kappa_0 \Delta x = (1, 2, 3)$.² For this first simulation, we take $\kappa_{\text{crit}} \Delta x \sim 1.2$. Regions where the opacities vary rapidly on the scale of a grid cell or less may be poorly approximated by our boundary condition, but are also underresolved in the two-moment scheme. A full MC evolution within these cells would not help much either, as our MC scheme assumes constant opacities and emissivities within any given cell. On the other hand, if the opacity varies on a length scale of more than 3 grid cells, our boundary condition should be accurate to better than 1%.

To gain more confidence in this choice, we perform a shorter simulation with $\kappa_{\text{crit}} \Delta x \sim 12$, and look at the neutrino distribution function above the neutron star ($z = 45$ km). We choose this point because the polar cap of the neutron star has the steepest opacity gradients, and we thus expect polar regions to be particularly sensitive to a bad choice of κ_{crit} . We find that differences between the two simulations for the flux of neutrinos, their energy spectrum, and their momentum distribution are close to the expected statistical noise, indicating that our boundary condition is not a dominant source of error at the accuracy currently reached by our code. Figure 1, for example, shows deviations in the pitch-angle and energy distribution of the neutrinos, normalized to the expected Poisson noise of *one* of the simulations (both simulations have similar Poisson noise). For an absolute error scale, we note that this figure was generated using $\sim(4300, 7400, 2200)$ packets per simulation for $(\nu_e, \bar{\nu}_e, \nu_x)$. We also measured differences in the average energy of the neutrinos of $\Delta\langle\epsilon\rangle = (0.15, 0.01, 0.7)$ MeV between the two simulations.

²We can also compute the ratio $|F|/E$, a measure of the anisotropy in the neutrino distribution function. For the same values of $\kappa_0 \Delta x$, we have $|F|/E \sim (0.056, 0.015, 0.005)$. These numbers are computed from the known analytical solution for this problem [62].

Our analysis of the MC results relies on two types of data. First, we have at our disposal the individual packets evolved by the MC scheme, and we log information about all MC packets leaving the computational domain. This allows us to obtain a MC estimate of the distribution function at any given point, as long as we compute it on-the-fly, and to post-process at will information about the neutrinos leaving the grid. Second, we compute time averages of moments of the neutrino distribution function. These are meant to be used, eventually, to provide a better closure to the two-moment scheme [41]. In this paper, they allow us to compare the M1 and MC results, and they also serve in the computation of the $\nu\bar{\nu}$ pair-annihilation rate. We use time-averaged moments so that a lower number of MC packets can be used in the simulation. This significantly reduces computational costs: in this study, the MC evolution is actually cheaper than the M1 evolution. With $\kappa_{\text{crit}} \Delta x \sim 1.2$ and each MC packet having an energy of $10^{-11} M_\odot c^2$, we have roughly as many MC packets on the grid as we have finite volume grid cells. All moments are computed by averaging over 100 MC packets (or one time step if more than 100 packets are present in a cell),³ leading to expected relative errors from Poisson noise of $\lesssim 10\%$.

B. Postmerger initial conditions

We choose as initial conditions the result of one of our existing simulations of merging neutron stars [44]. The initial binary is an equal mass, nonspinning system. Each neutron star has an ADM mass of $1.2 M_\odot$ in isolation. The neutron star matter is described by the equation of state of Lattimer and Swesty [63] with nuclear incompressibility parameter $K_0 = 220$ MeV (LS220). We use the publicly available NuLib table providing the fluid properties as a function of density (ρ), temperature (T), and electron fraction (Y_e) for this equation of state [64]. In this work, we begin from a snapshot of the simulation 10 ms after merger, and evolve the postmerger remnant for 4.5 ms. This is longer than the dynamical timescale of the remnant neutron star, but shorter than the cooling timescale of the remnant.

The fluid properties within poloidal and equatorial slices through the remnant are shown in Fig. 2. The central object is a hot, differentially rotating, massive neutron star. It is surrounded by a thick accretion disk with temperature $T \sim 5\text{--}10$ MeV and electron fraction $Y_e \sim 0.1\text{--}0.3$. Shocked spiral arms driven by the rotation of the distorted neutron star are visible in the disk. Low-density outflows are observed in the polar regions. Neutrino emission and absorption make these outflows relatively proton rich ($Y_e \sim 0.3\text{--}0.5$). In previous work, we demonstrated that the composition of these outflows is quite sensitive to the method used to compute the average energy of the

³The exact procedure to compute time-averaged moments is described in [41].

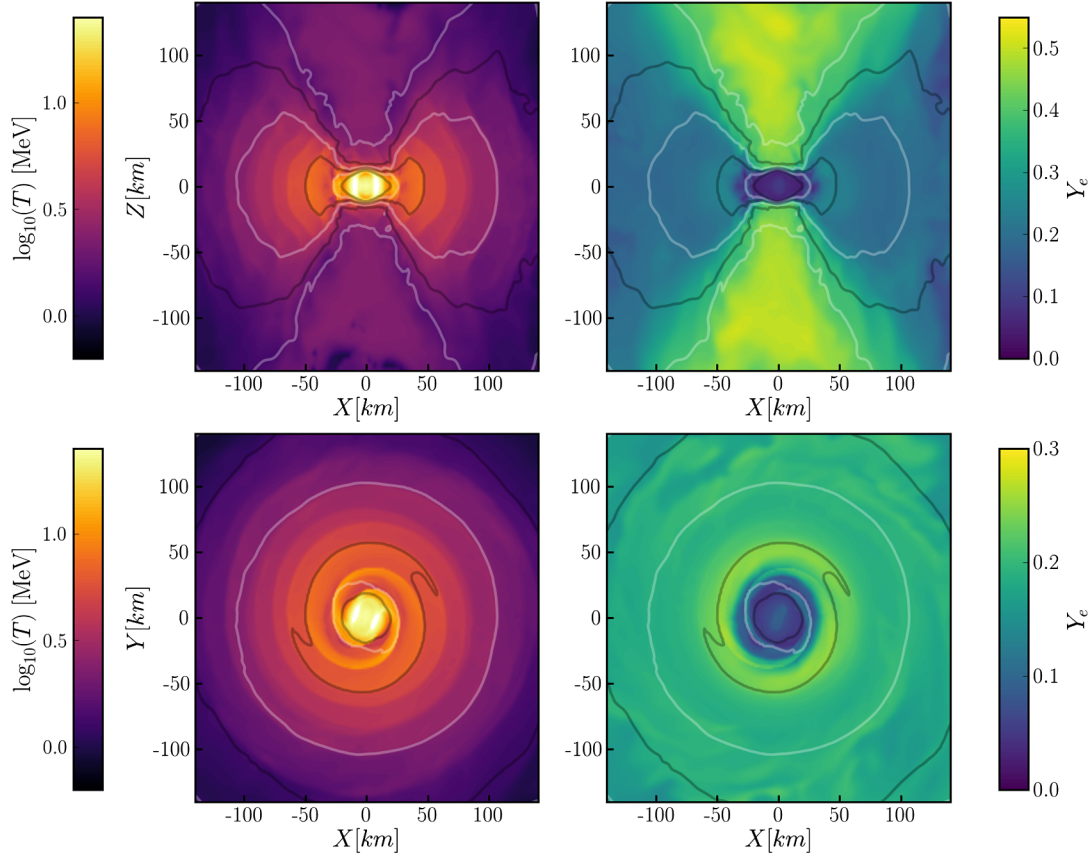


FIG. 2. Poloidal (top) and equatorial (bottom) slices through the merger remnant. In each figure, solid lines show density contours of $\log_{10}(\rho/[1 \text{ g/cm}^3]) = (8, 9, 10, 11, 12, 13, 14)$. Color scales show the fluid temperature (left) and electron fraction (right).

neutrinos [44]. The starting point of this study is a simulation using our best energy estimate so far for neutrino energies, i.e., the estimate obtained by evolving both the neutrino number density and the neutrino energy density.

Our existing simulation provides us with initial conditions for the metric, the properties of the fluid, and the moments of the neutrino distribution function evolved by the M1 scheme. These have to be complemented with initial conditions for the MC evolution. At the initial time, we randomly draw particles from a thermal distribution in equilibrium with the fluid. While this is a fairly reasonable assumption in the most optically thick regions evolved by the MC algorithm, this is clearly inexact in semitransparent and optically thin regions. The duration of the simulation is chosen to allow MC packets to diffuse from the surface of moderate optical depth below which we do not use the MC algorithm (discussed in the previous section), and then travel to the boundary of the domain. In the rest of this paper, we largely ignore the first ~ 3 ms of evolution, and focus solely on times when we expect that the properties of the MC packets are no longer influenced by our choice of initial conditions.

C. Numerical grids

We set our numerical grids as in [44]. The pseudospectral grid on which we evolve Einstein’s equations is constructed

from a small filled sphere centered on the neutron star remnant, surrounded by 59 spherical shells. The number of basis functions within each subdomain is chosen so that the truncation error in the metric and in its spatial derivatives is less than 5×10^{-4} . Given the near-spherical symmetry of the high-density regions of the postmerger remnant, this requires only $\sim 140k$ grid points.

The finite volume grid on which we evolve the equations of hydrodynamics and the moments of the neutrino distribution function is constructed from 4 levels of refinement. The finest level has a grid spacing $\Delta x \sim 300$ m. At each subsequent level, the grid spacing is multiplied by 2. All levels have the same number of grid cells, $200 \times 200 \times 100$, and are centered on the neutron star remnant. Each level is further subdivided into 144 patches, for parallelization. Each patch is then extended by 3 ghost cells in each direction, for reconstruction of the fluid variables from grid centers to faces. Overall, the grid has 576 patches and a total of ~ 28 million cells. As we aim to estimate differences between the MC and M1 schemes for a fixed setup and at a limited computational cost, we do not attempt to vary the grid spacing or test the convergence of the fluid evolution. Our grid spacing is fairly typical for neutron star merger simulations with SpEC, and can capture the dynamics of the postmerger remnant [44]. Our grid would, on the other hand,

be far too coarse to study the effects of magnetic fields [65], which are entirely ignored in this work.

III. NEUTRINO MOMENTS AND DISTRIBUTION FUNCTION

A. Overview: Polar and equatorial moments

Before beginning our detailed analysis of the M1 and MC results, it is useful to examine the global properties and spatial distribution of the neutrinos in our simulations. Table I lists important overall properties of the neutrinos leaving the grid. We see, in particular, that $\bar{\nu}_e$ is the dominant type of neutrino emitted by the remnant, both in terms of energy and number emission (note that ν_x values should be divided by 4 to get per-species results). We also observe the usual hierarchy of temperatures, with ν_x being hotter than $\bar{\nu}_e$ neutrinos, which are themselves hotter than ν_e . Global quantities show relative differences of (10–20)% between the M1 and MC results, which could be due either to the approximations made in the M1 scheme or to the slightly different microphysics implemented in each algorithm. We also note that the net flux of lepton number in the two schemes (i.e., number of ν_e minus number of $\bar{\nu}_e$ leaving the grid) would likely be in closer agreement if the MC scheme was coupled to the fluid, as the fluid would evolve towards a new, slightly modified equilibrium composition.

TABLE I. Global properties of the neutrino emission 14 ms after merger, according to the M1 and MC algorithms. The average energy is weighted by the number of neutrinos. The effective temperature and spectral index are defined by Eq. (19), and cannot be computed in the (gray) M1 algorithm. Note that ν_x values are for all 4 heavy-lepton species combined. The M1 and MC schemes use slightly different definitions of global quantities: the M1 scheme measures the total energy leaving the grid and computes average energies as observed by an inertial observer at the domain boundary, while the MC scheme measures the total number of particles leaving the grid and estimate the average energy of particles in a packet to be p_t , an estimate of the energy of the packets at infinity. These differences could explain mismatches of order $|1 - \alpha| \sim (2 - 3)\%$ between the M1 and MC results, but not the observed (10–20)% mismatches.

| | ν_e | $\bar{\nu}_e$ | ν_x |
|---|---------|---------------|---------|
| M1 scheme | | | |
| Luminosity [10^{52} erg/s] | 5.8 | 11 | 11 |
| Number flux [$10^{57}/s$] | 3.4 | 5.1 | 2.6 |
| Average energy [MeV] | 10.6 | 13.4 | 26.4 |
| MC scheme | | | |
| Luminosity [10^{52} erg/s] | 5.0 | 10 | 11 |
| Number flux [$10^{57}/s$] | 2.7 | 4.0 | 2.9 |
| Average energy [MeV] | 11.3 | 15.5 | 23.0 |
| Effective temperature $T_{(\nu)}$ [MeV] | 1.9 | 2.7 | 9.0 |
| Spectral index α | 4.8 | 4.6 | 1.5 |

Figure 3 shows the energy density, average radial velocity, and radial component of the pressure tensor along the vertical z axis and along the x axis, at the end of our simulation. The neutrino energy density is largest in the optically thick regions at the center of the star for $\bar{\nu}_e$ and ν_x , while ν_e are suppressed in the neutron star core: ν_e are immediately absorbed by the neutrons in the hot, protonizing core. Along the vertical direction, a secondary peak in the neutrino energy density is observed on the hot surface of the neutron star, while in the equatorial plane, peaks in the neutrino distribution function are associated with the hot, shocked tidal arms in the disk. At large distances, the energy density falls as r^{-2} , as expected. The neutrino density far from the remnant is about 3 times as large at the poles as on the equator, and dominated by $\bar{\nu}_e$ everywhere. Note that $\bar{\nu}_e$ are the most abundant species because the equilibrium composition of the remnant is at a higher Y_e than its initial composition. The agreement between M1 and MC appears to be quite good for ν_e and $\bar{\nu}_e$, and for ν_x everywhere but at the poles, where the M1 code overestimates the neutrino energy density by a factor of 2.

The average radial velocity of the neutrinos (F_{\parallel}/E) vanishes in the optically thick, rotating core, then rapidly grows as the neutrinos decouple from the fluid. This decoupling occurs over a short range of radii in the vertical direction. Differences between species are more noticeable in the horizontal plane: ν_x decouple closer to the core, then $\bar{\nu}_e$, and finally ν_e . In optically thin regions, F_{\parallel}/E is an indicator of the width of the distribution of neutrino pitch angle (the angle between the direction of propagation of the neutrinos and the radial direction). Here, $F_{\parallel}/E \sim 1$ indicates that all neutrinos propagate along the radial direction, while lower values indicate less forward-peaked distributions. We see that F_{\parallel}/E grows to the speed of light as the distance to the source increases, and the remnant effectively becomes a point source. While qualitative agreement between the MC and M1 results is still observed, the growth of F_{\parallel}/E in the vertical direction is faster in the M1 code—i.e., the M1 code expects the distribution of neutrinos to be more forward-peaked than in the MC code.

Differences between the M1 and MC results are more apparent in the pressure tensor, particularly in the polar regions. Just above/below the remnant, the MC code finds $P_{\parallel}/E \sim 0.6$ – 0.8 , while the M1 code finds $P_{\parallel}/E \sim 1$. We argue in the next sections that these differences are due to the inability of the M1 code to handle converging streams of neutrinos, even though converging neutrinos are an expected feature of the polar regions. In optically thick regions, the M1 and MC codes agree, but that should not be a surprise: there, both codes are constructed to enforce equilibrium between neutrinos and the fluid.

Figure 4 continues our description of the neutrinos along the x axis and z axis, by showing the average energy of the neutrinos as measured by an inertial observer, $\langle \epsilon \rangle = E/N$.

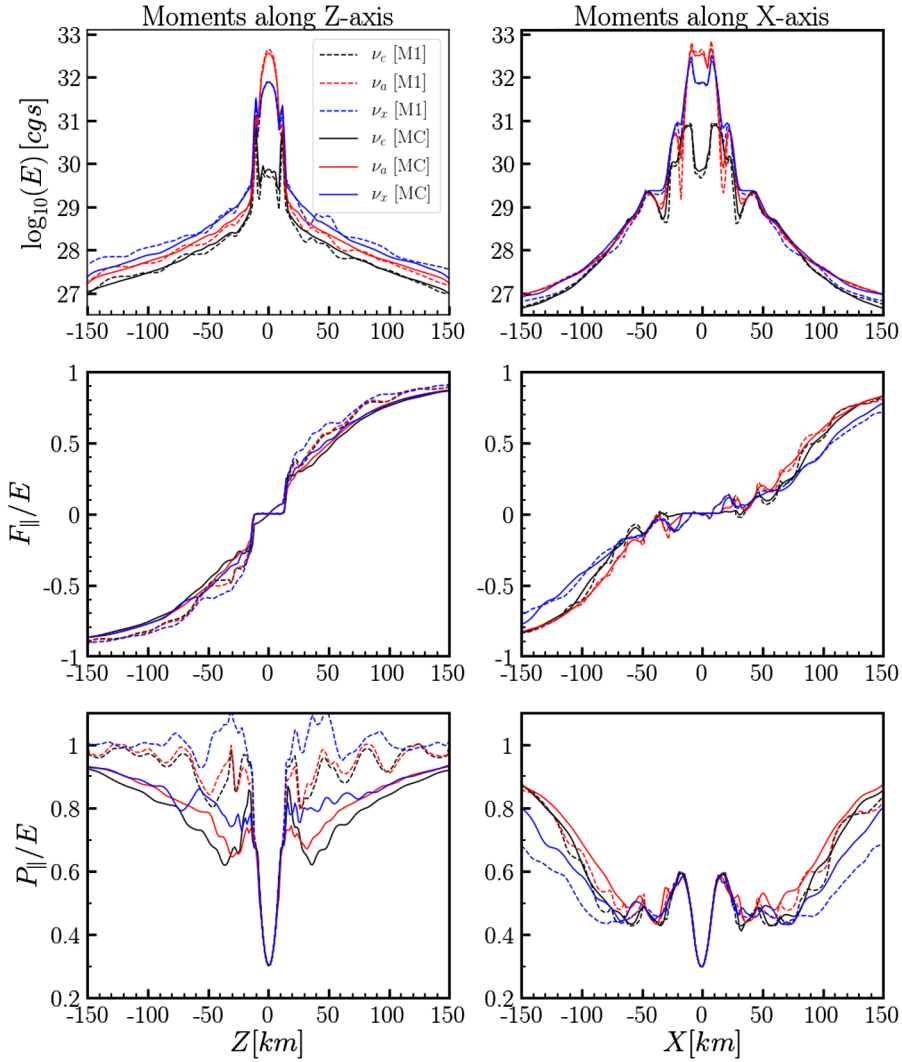


FIG. 3. One-dimensional profiles of the neutrino moments in the MC (solid lines) and M1 (dashed lines) code for each species of neutrinos (ν_x values are for all heavy-lepton neutrinos combined), 14 ms after merger. We show the energy density (top), the parallel (radial) component of the normalized transport flux (average velocity of the neutrinos, middle), and the parallel component of the Eddington tensor (bottom) along the z axis (left) and x axis (right). M1 values are computed by interpolation, while MC moments are computed using all packets within a ball of radius of $300 \text{ m} + 0.05 * R$ centered on the desired point, with R the distance to the center of the remnant. All values are computed in the inertial frame, without projection into an orthonormal frame (hence the few points where $P_{\parallel} > E$).

Neutrino energies are naturally large in the hot neutron star core (50–100 MeV), and in other optically thick hot regions (e.g., shocked tidal arms). However, lower-energy neutrinos have a higher probability to escape the remnant, and the average energy of the escaping neutrinos is $\sim 10\text{--}30$ MeV (with ν_x hotter than $\bar{\nu}_e$, which are themselves hotter than ν_e). While the M1 and MC codes agree on the general hierarchy of temperatures, pointwise estimates of the neutrino energies can differ by up to $\sim 30\%$ between the two algorithms. We will show later that agreement is a little better when considering time-averaged or spatially averaged $\langle \epsilon \rangle$. In particular, large oscillations in the average energies computed using the M1 code may be a sign of other undesirable effects of approximate transport.

Finally, Fig. 5 shows the energy density of neutrinos along a line 25° from the polar axis (in the Oxz plane). As along other directions, agreement between the M1 and MC codes is good in optically thick regions. However, we now see significant disagreement in optically thin regions, with up to a factor of ~ 2 more neutrinos measured in the M1 code than the MC code. We thus see that the agreement observed along the polar axis and the x axis is in no way universal. We discuss these differences in more detail in the following sections.

B. Eddington tensor

We now consider the impact of one of the main assumptions of the two-moment scheme: the Minerbo

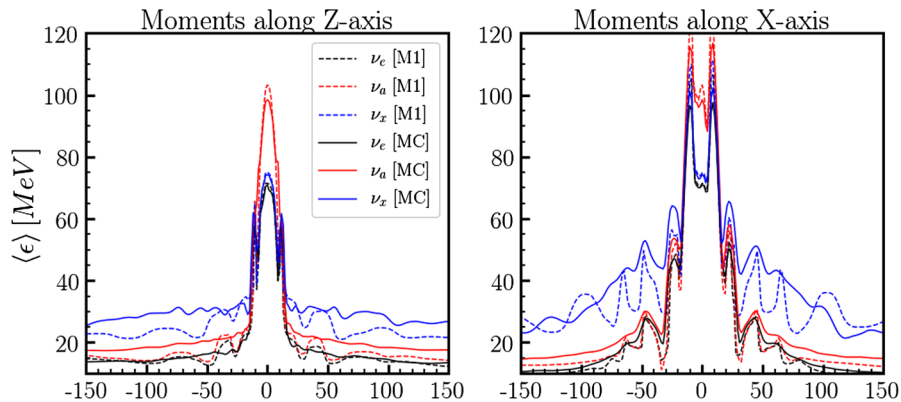


FIG. 4. Same as Fig. 3, but for the average energy of the neutrinos in the inertial frame.

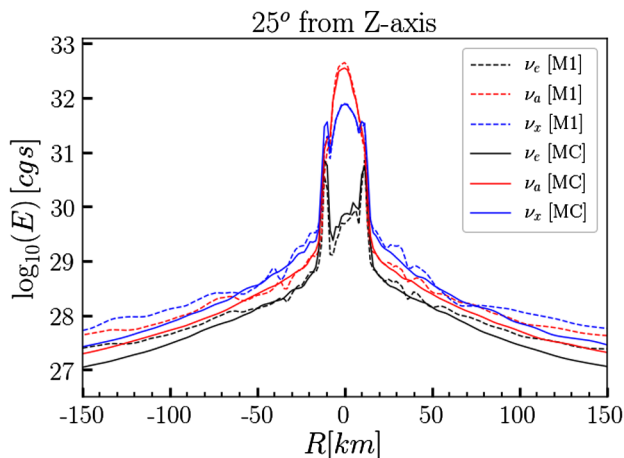


FIG. 5. Energy density of neutrinos for all species in the M1 and MC codes, along a line 25° from the polar axis.

analytical closure. In Figs. 6 and 7, we show equatorial and poloidal slices through the merger remnant, as for the fluid quantities plotted in Fig. 2. The figures show various components of the Eddington tensor $f_{ij} = P_{ij}/E$, in an orthonormal frame constructed by an inertial observer applying the Gram-Schmidt algorithm to vectors tangent to spatial coordinate lines. For each component we plot the MC results, and the difference between MC and M1 results. Here, the MC moments are calculated as they would be if we coupled the MC and M1 schemes, i.e., by time averaging over all packets passing through a given grid cell. From the MC results, we see that statistical errors, roughly approximated as the noise in the MC predictions, are at the level of a few percent, slightly better than expected.

The difference between MC and M1 is largest in the polar regions, and for f_{zz} . Errors of 0.1–0.3 are the norm within a few neutron star radii of the surface of the remnant, with the Minerbo closure consistently returning larger values of f_{zz} than the MC closure. That the Minerbo closure is particularly inaccurate in polar regions is no

surprise: neutrinos emitted by the hot neutron star and the accretion disk cross paths there, and will create artificial radiation shocks when the Minerbo closure is used. With this simulation, we can quantify this long-standing assumption. We find that errors in the polar regions are very significant: the MC results indicate that $f_{zz} \sim 0.5$ – 0.7 at points where the difference between MC and M1 is $|\Delta f_{zz}| \sim 0.1$ – 0.3 . Outside of the polar regions, we observe differences $|\Delta f_{ij}| \lesssim 0.1$. In some of these regions, the difference between the MC and M1 results is consistently of the same sign, and thus does not appear due to statistical noise in the MC results. Regions with rapid variations in the error measurements (with typically $\Delta f_{ij} \lesssim 0.03$), on the other hand, most likely have larger MC errors than M1 errors. This is the case in most of the accretion disk, at least at radii $r \lesssim 70$ km.

Overall, the Minerbo closure appears to do quite well in the optically thick and semitransparent regions where most of the neutrinos are emitted, but has some clear issues farther from the remnant, where we pay for the inaccuracies of the optically thin analytical closure. Large errors for the closure in the polar regions have a couple of potentially important consequences for neutrino-matter interactions in these systems. One is that the spatial distribution of neutrinos in optically thin regions is inaccurate when using a M1 scheme. This impacts the resulting rate of absorption of ν_e and $\bar{\nu}_e$, and thus the evolution of the composition of polar outflows. We study the spatial distribution of neutrinos in more detail in Sec. III D. Another consequence is that the inferred energy deposition from $\nu\bar{\nu}$ annihilations in polar regions may be difficult to accurately estimate when using the M1 scheme. We consider that problem in Sec. IV.

C. Pointwise distribution function of neutrinos

To better understand the momentum-space distribution of neutrinos, we now look at their direction of propagation and their energy spectrum at individual points. As opposed to our computation of the Eddington tensor, we do not perform any time averaging here. Instead, we study the

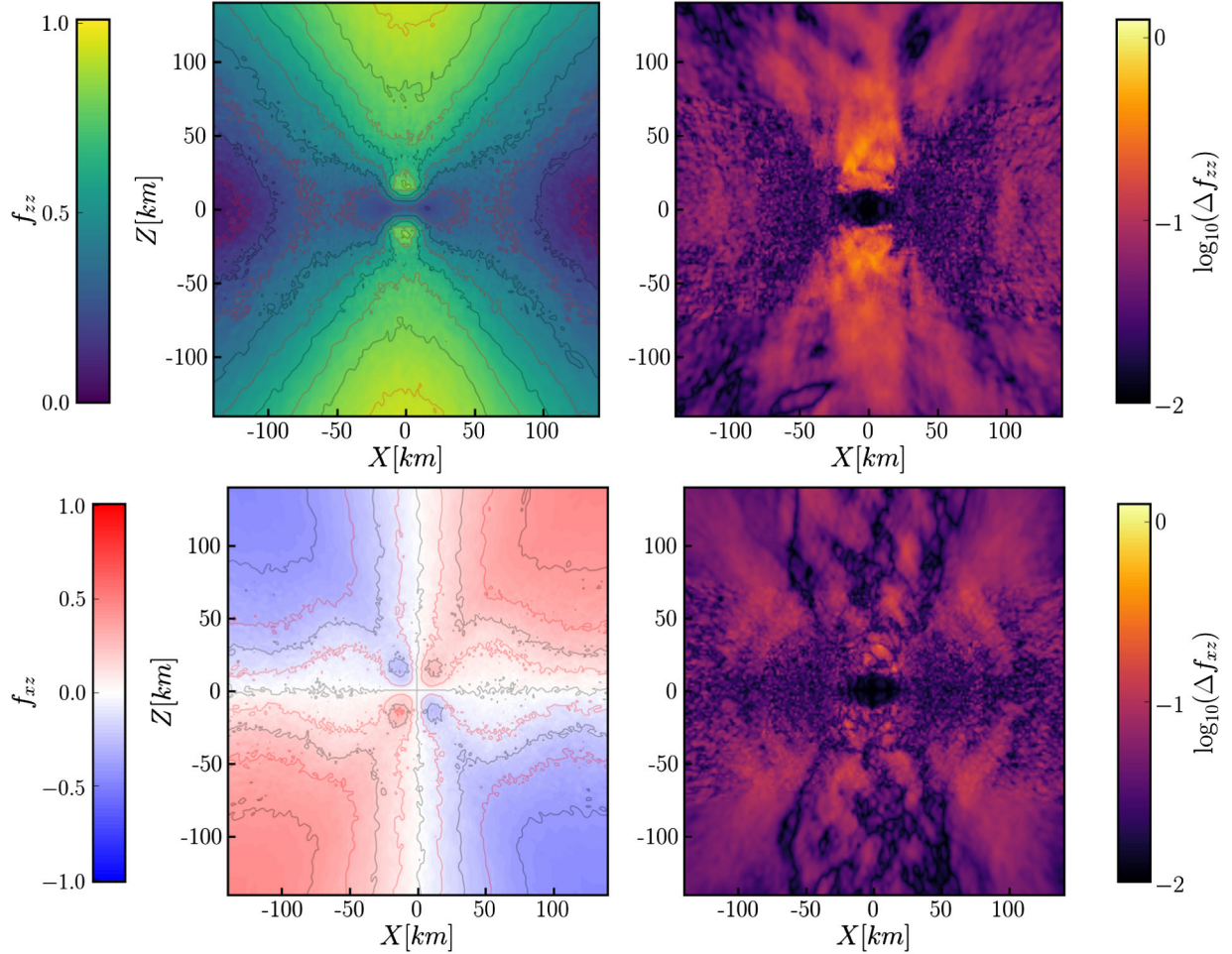


FIG. 6. Poloidal slice through the merger remnant. The left column shows the diagonal and off-diagonal components of the Eddington tensor f_{zz} and f_{xz} as measured with the MC code. Solid lines are contours of f_{zz}, f_{xz} separated by 0.1 (alternating red and black lines). This provides an order-of-magnitude estimate of the statistical noise, with $\Delta f_{\text{stat}} < 0.05$. The right column shows the difference between the MC and M1 Eddington tensors. In the massive neutron star, the difference is negligible. In the disk, it is dominated by statistical MC noise. Outside of the remnant, large errors in the Minerbo closure dominate. In particular, $\Delta f_{zz} \sim 0.1\text{--}0.3$ in the polar regions. All results are for ν_e neutrinos.

properties of all MC packets within a distance Δd of a point \mathbf{x}_i at a fixed time t_i , following the procedure outlined after Eq. (17). We also limit ourselves to optically thin regions, where differences between the M1 and MC results are significant. As the distribution function of neutrinos at a given time is 6 dimensional, and different physical processes will require the visualization of that distribution function in different ways, we do not attempt to provide a complete view of the distribution function. We limit ourselves to some notable properties of the distribution function, provided as examples of what information can be gleaned from our MC results.

At each point, the momentum of neutrinos is characterized by the parameters (ϵ, θ, ϕ) , where ϵ is the energy of the neutrinos measured by an inertial observer, θ the angle between the momentum of the neutrinos and the radial coordinate in an orthonormal tetrad constructed by an

inertial observer (pitch angle), and ϕ an azimuthal angle for rotation around that same radial axis. We first consider points along the polar axis, at $z = (45, 90, 135)$ km. At all 3 points, we find a flat distribution in ϕ (see Fig. 8), within statistical errors and after marginalizing over (ϵ, θ) . This indicates that deviations from axisymmetry in the hot neutron star and in the surrounding accretion disk do not have a significant impact on the neutrino distribution function at the poles. This result is particularly interesting if we aim to use time-averaged MC moments to close the two-moment evolution equations. It may be sufficient for the averaging timescale to be short compared to the thermal evolution timescale of the remnant, rather than its orbital timescale.

Figure 9 shows the probability distribution of neutrinos with respect to θ . As expected, it becomes more forward-peaked as we move away from the remnant. We can

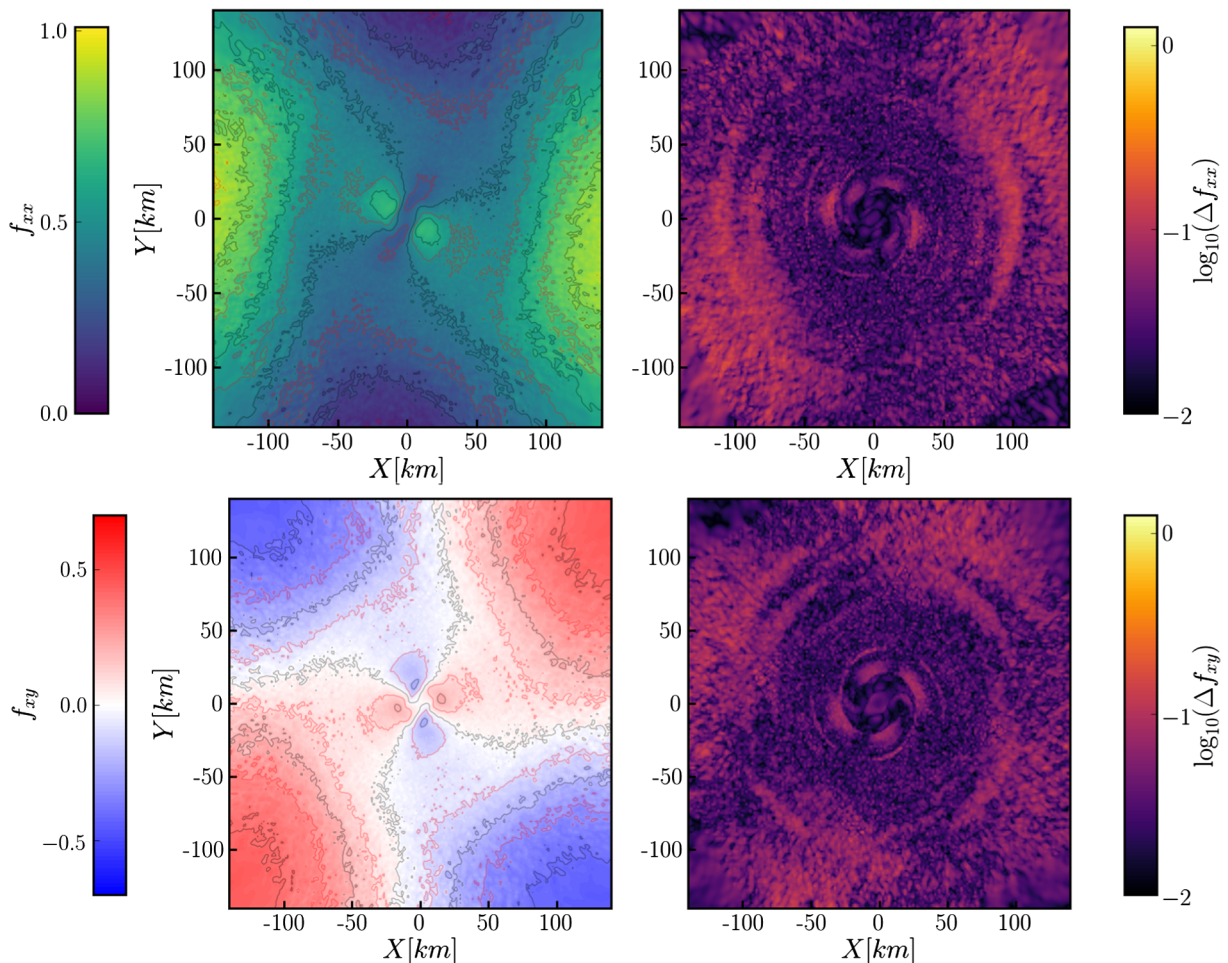


FIG. 7. Same as Fig. 6, but for an equatorial slice through the remnant, and showing components f_{xx} , f_{xy} of the Eddington tensor. The Minerbo closure is significantly more accurate here than in the polar regions, although some regions of the shocked spiral arms show consistent biases in the Minerbo closure at a level $\Delta f_{ij} \sim 0.1$.

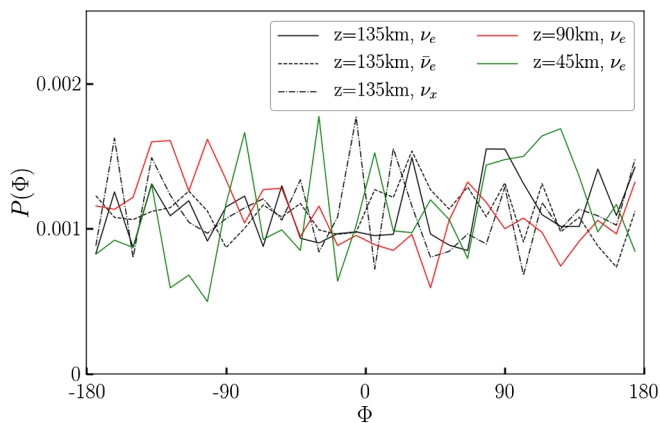


FIG. 8. Distribution probability of neutrinos as a function of the azimuthal angle ϕ of their 4-momentum, at different points on the polar axis. We sample all packets within $\Delta d = 0.1z$ of the target point. We have 400–2000 packets within each region and for each type of neutrino.

also see clear differences between neutrino species. The pitch-angle distribution is narrower for the heavy-lepton neutrinos, and wider for $\bar{\nu}_e$. For ν_e , the distribution function peaks at $\theta \sim 45^\circ$ rather than $\theta \sim 0^\circ$. This is due to the relative contribution of the neutron star and accretion disk to the neutrino fluxes. Nearly all ν_x are coming from the neutron star, while the disk contributes significantly to the production of $\bar{\nu}_e$ and ν_e . The broad distribution of $f(\theta)$ does not match the assumptions made by the M1 scheme in these regions.

Finally, the energy spectrum of neutrinos is shown in Fig. 10. The shift in the spectrum as we move away from the remnant is too large to be due to gravitational redshift alone. We expect a $\sim 6\%$ shift in the average energy of the neutrinos between $z = 45$ km and $z = 135$ km, but observe a 20% change between those points. The cooler spectrum at large radii is a geometrical effect, accounting for a larger fraction of the polar neutrinos coming from the disk rather than the hotter neutron star as we move away from the remnant along the polar axis. The spectra also

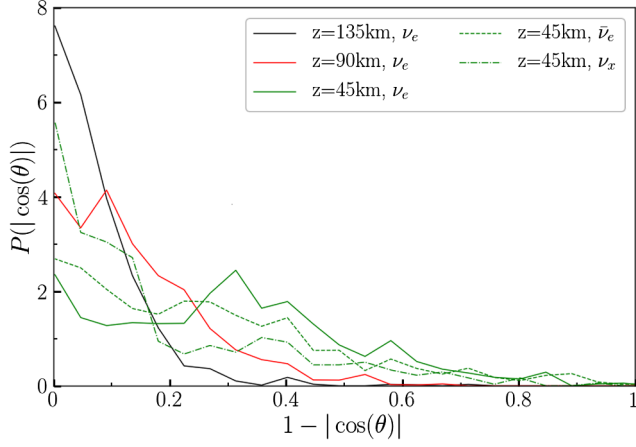


FIG. 9. Same as Fig. 8, but for the distribution probability with respect to $\cos(\theta)$, with θ the neutrino pitch angle. We show multiple species for the closest point to the remnant, as the angular distribution is more sensitive to the finite size of the emitting region close to the remnant.

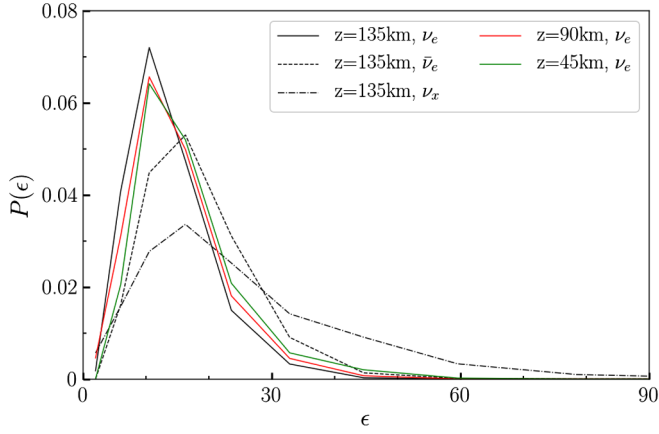


FIG. 10. Same as Fig. 8, but for the distribution probability with respect to the neutrino energy ϵ . We use 12 energy bins to generate this figure, identical to the bins of the NuLib table.

show that the assumption of a blackbody (or softer) spectrum made in the gray moment scheme [44] is not accurate. We fit the normalized spectra at $z = 135$ km to the function

$$f(\epsilon, T_{(\nu)}, \alpha) = \frac{\epsilon^\alpha}{T_{(\nu)}^{\alpha+1} \Gamma(\alpha-1)} e^{-\epsilon/T_{(\nu)}}. \quad (19)$$

For a blackbody spectrum, and approximating the Fermi-Dirac distribution of neutrinos by a Boltzmann distribution, we would expect $\alpha = 2$, and $T_{(\nu)}$ would be the temperature of the neutrinos. Instead, for $(\nu_e, \bar{\nu}_e, \nu_x)$ we find $\alpha = (4.2, 4.3, 1.7)$ and $T_{(\nu)} = (2.5, 3.3, 9)$ MeV. The neutrino spectrum is thus significantly harder than expected for ν_e and $\bar{\nu}_e$, and closer to a blackbody for heavy-lepton

neutrinos. The average energy of polar neutrinos evaluated from the gray moments (E, F_i, N) , on the other hand, is quite close to the average energy measured in the MC code: the average energy of neutrinos leaving the grid with a momentum misaligned by less than 30° with respect to the polar axis, as measured in the moment scheme, is within 10% of the MC results.

Given the expected dependence of the absorption and scattering opacities of neutrinos in the square of the neutrino energies, we can estimate that these different spectral shapes would lead us to underestimate reaction rates for ν_e and $\bar{\nu}_e$ by up to $\sim 15\%$, if the average energy of neutrinos was accurately estimated. As the average energy of the polar neutrinos is within 10% of the MC results in the M1 scheme, absorption and scattering opacities in the polar regions will be accurate within $\sim 30\%$. We note that this is only true because we evolve the neutrino number density in the M1 scheme, thus obtaining a reasonably accurate local estimate of the average neutrino energy. If we had approximated the neutrino energy spectrum by a blackbody distribution at the fluid temperature $[T_{(\nu)} \sim (2-3)$ MeV, $\alpha = 2]$, the average neutrino energies would have been off by factors of 2–5.

We also study the properties of the neutrino distribution function at points farther away from the polar axis, in the $y = 0$ plane (i.e., the poloidal slice shown in Fig. 2). We consider the points

$$(x, z) = [(45, 135), (90, 135), (135, 135), (135, 90), (135, 45), (135, 0)] \text{ km}. \quad (20)$$

While at those points the probability distribution with respect to the angle ϕ is no longer isotropic, the only asymmetries observed in the neutrino distribution function are the expected preference for neutrinos to come from the equatorial plane of the remnant, and a more forward-peaked distribution function at larger distances. This is consistent with what we observed in the polar regions, and with our assumption that the neutrino distribution function does not vary significantly over the rotation period of the remnant. The spectrum of the neutrinos remains well fitted with the same function as in the polar regions, with a hard spectrum ($\alpha \in [4, 5]$) for ν_e and $\bar{\nu}_e$ and a near blackbody spectrum for ν_x . The accuracy of the M1 results for ϵ decreases significantly as we move away from the polar axis. We find relative errors of (10–30)% in the average neutrino energies, which could lead us to use absorption/scattering opacities that are wrong by about of a factor of 2. In these regions, however, the composition of the fluid is not as sensitive to estimates of ϵ as closer to the poles [44]. The impact of this error on EM observables is thus likely to be reasonably small, compared to other existing simulation errors.

Overall, we estimate that the errors in the scattering and absorption opacities computed in the two-moment scheme

are likely $\lesssim 30\%$ in the polar regions, where they impact EM observables the most. Errors are larger farther away from the poles, but this may not matter as much for modeling EM signals. However, computing the opacities is only one part of the problem. The energy density of neutrinos also impacts the reaction rate for neutrino-matter interactions. We show in Sec. III D that this is a more significant issue.

D. Properties of escaping neutrinos

We now consider the properties of the neutrinos leaving the computational domain, starting with their energy spectrum. This illustrates differences between the energy of the neutrinos in the M1 and MC schemes, already discussed in the previous section. The spectrum of escaping neutrinos 14 ms after merger is shown on the left panel of Fig. 11, for all three types of neutrinos. We bin the spectrum using the same 12 energy bins as in the NuLib table. It is worth noting, however, that our ability to resolve the energy distribution of neutrinos is understated in this plot. All MC

packets are emitted with the energy of the center of a bin, but their energies can then be shifted due to gravitational and velocity redshift as well as scattering events, so that, for example, a global shift of the spectrum by a fraction of an MeV would be captured by the MC code.

As for the pointwise data, the energy spectrum of ν_e and $\bar{\nu}_e$ is well fitted by Eq. (19) with a hard spectral index ($\alpha = 4.8$ and $T_{(\nu)} = 1.9$ MeV for ν_e ; $\alpha = 4.6$ and $T_{(\nu)} = 2.7$ MeV for $\bar{\nu}_e$). The spectrum of heavy lepton neutrinos is slightly softer than a blackbody ($\alpha = 1.5$, $T_{(\nu)} = 9.0$ MeV). The average energy of escaping neutrinos is reasonably well estimated in the moment scheme for ν_e and $\bar{\nu}_e$ (1–2 MeV errors), while larger errors are observed for ν_x (4 MeV).

The right panel of Fig. 11 shows starker differences between the M1 and MC results. There, we show the probability distribution of neutrinos as a function of their latitude in a spherical polar coordinate system with axis aligned with the angular momentum of the remnant. Artificial shocks cause neutrinos to accumulate close to

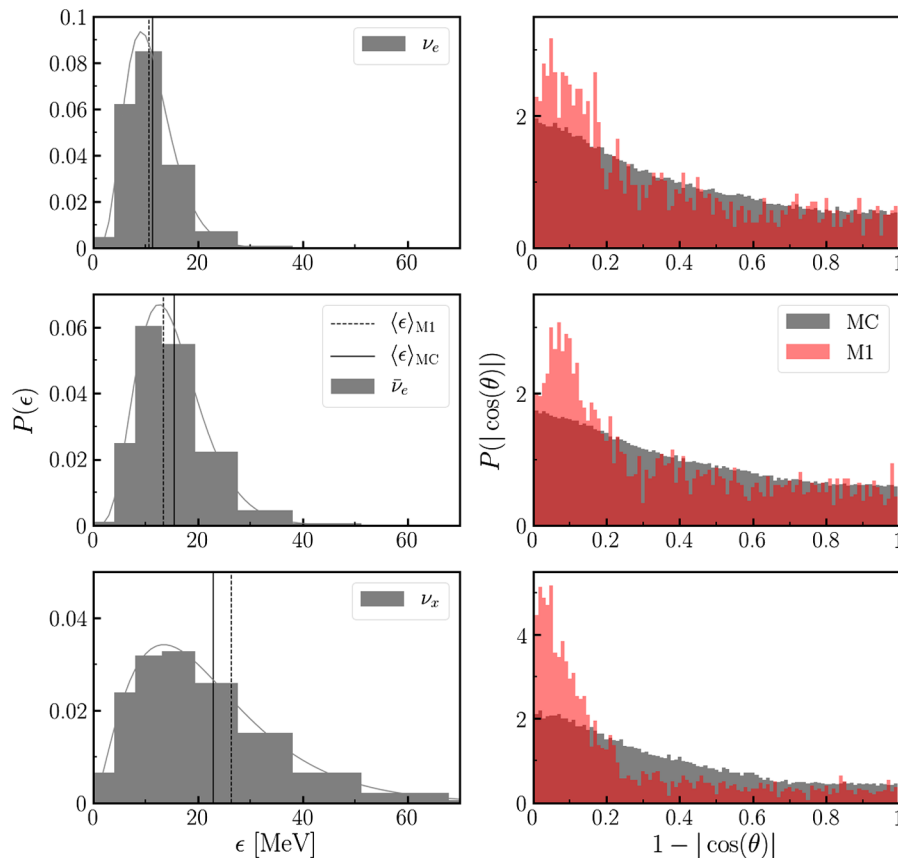


FIG. 11. Left: Energy distribution of the neutrinos leaving the computational domain (measured on the surface of a parallelepiped 6 grid spacings from the subdomain boundary, i.e., approximately a parallelepiped of size $[480 \times 480 \times 240]$ km centered on the origin), for all 3 species of neutrinos. In each plot, the dashed vertical line shows the average neutrino energy estimated by the M1 scheme, and the solid vertical line the same quantity estimated by the MC scheme. The solid grey line shows our best fit to the spectrum. Right: Angular distribution of the neutrinos leaving the grid. Here, θ is the usual spherical-polar coordinate, not the pitch angle of the neutrinos. Grey histograms show the MC results, and red histograms the M1 results. Errors in the Minerbo closure lead to a large overestimate of the neutrino density in the polar regions. In all plots, we integrate the neutrino fluxes over a $50 \mu\text{s}$ interval 14 ms after merger.

the polar axis in the M1 code, an effect that is avoided in the MC code. This results in an excess of neutrinos in the polar regions ($\theta \lesssim 35^\circ$), by $\sim 50\%$ for ν_e and $\bar{\nu}_e$ and by nearly a factor of 2 for ν_x . This excess is likely to have a more important impact on the evolution of the polar outflows than the other sources of errors considered so far. The absorption rate of all flavors of neutrinos is significantly boosted in M1 simulations, causing excess heating of the outflows. The effect of this error on the composition of the outflows is hard to determine with certainty. Generally speaking, overestimated neutrino-matter reaction rates and fluid temperatures are likely to lead us to overestimate the electron fraction of the outflows in the M1 code. Quantifying this error will require simulations in which the MC scheme is fully coupled to the moment evolution (or directly to the fluid).

IV. $\nu\bar{\nu}$ PAIR ANNIHILATION

So far, we have discussed aspects of neutrino transport and neutrino-matter interactions that are approximately modeled in M1 simulations. We now move to a potentially important physical effect that is entirely ignored in our existing M1 simulations: $\nu\bar{\nu} \rightarrow e^+e^-$ pair annihilation in low-density polar regions. Existing estimates indicate that pair annihilation can deposit enough energy in the polar regions to drive mildly relativistic outflows, and clear the poles of most baryons—although on their own they are probably not sufficient to power anything but the weakest short gamma-ray bursts [35–38,40]. Pair annihilation has been included in 2D postmerger simulations using the two-moment approximation [37,39], and by post-processing late-time snapshots of a postmerger remnant [40], but not in self-consistent 3D simulations of these systems. One reason is that energy deposition due to pair annihilation is strongly dependent on moments of the neutrino distribution function that are not evolved by the M1 scheme, mainly because counterpropagating neutrinos have a much higher annihilation cross section than neutrinos propagating in the same direction.

To study this effect, let us follow Fujibayashi *et al.* [38] and assume that the phase-space blocking factors and masses of electrons and positrons are negligible. This is nearly certainly a good approximation in the low-density polar regions where pair annihilation plays an important role. The heating rate $Q_{\text{pair},\nu_i}^{(+)}$ due to the neutrino species ν_i can then be computed as a function of the moments of the neutrino distribution function through an integral over the phase space of neutrinos and antineutrinos (see [35,38]). If the energy in the fluid frame $\omega_{(\nu_i)}$ can be factored from this integral and approximated by the average energy $\langle\omega_{(\nu_i)}\rangle_{\text{pair}}$ of neutrinos ν_i , then

$$Q_{\text{pair},\nu_i}^{(+)} = \frac{C_{\nu_i\bar{\nu}_i}^{\text{pair}} G_F^2}{3\pi\hbar^4 c^3} \langle\omega_{(\nu_i)}\rangle_{\text{pair}} (J\bar{J} - 2H^\mu\bar{H}_\mu + S^{\mu\nu}\bar{S}_{\mu\nu}) \quad (21)$$

with $G_F \approx 4.5438(\hbar c)^3 \text{erg}^{-2}$ the Fermi constant, $(\bar{J}, \bar{H}^\mu, \bar{S}^{\mu\nu})$ fluid-frame moments of antineutrinos,

$$C_{\text{pair}} = 1 \pm 4 \sin^2(\theta_W) + 8 \sin^4(\theta_W) \quad (22)$$

(with the plus sign for electron neutrinos and the minus signs for heavy-lepton neutrinos), and $\sin^2 \theta_W \approx 0.2319$. The total heating rate due to pair annihilation is then

$$Q_{\text{pair,tot}}^{(+)} = Q_{\text{pair},\nu_e}^{(+)} + Q_{\text{pair},\bar{\nu}_e}^{(+)} + 4Q_{\text{pair},\nu_x}^{(+)}, \quad (23)$$

where the only difference between $Q_{\text{pair},\nu_e}^{(+)}$ and $Q_{\text{pair},\bar{\nu}_e}^{(+)}$ due to different average energies $\langle\omega_{(\nu_i)}\rangle_{\text{pair}}$ for ν_e and $\bar{\nu}_e$. The neutrino annihilation number rate is naturally the same for ν_e and $\bar{\nu}_e$. Equation (21) can be seen as a definition for the average energy $\langle\omega_{(\nu_i)}\rangle_{\text{pair}}$, yet computing that average energy from information available in the M1 scheme is not possible. Even in the MC algorithm if we want to compute the annihilation rate from the stored moments of the neutrino distribution function rather than by direct interaction between every pair of neutrino packets, we do not currently store enough information to exactly compute $\langle\omega_{(\nu_i)}\rangle_{\text{pair}}$. If neutrinos of different energies all have the same angular distribution, $\langle\omega_{(\nu_i)}\rangle_{\text{pair}}$ is the energy-weighted average energy of neutrinos (rather than the number-weighted average energy $\langle\epsilon\rangle$ used in earlier sections). If neutrinos of different energies have different angular distributions, however, there is no simple way to compute $\langle\omega_{(\nu_i)}\rangle_{\text{pair}}$. Considering that low-energy neutrinos are more likely to come from the accretion disk and thus have a higher annihilation cross section, it is quite likely that using the energy-weighted average energy slightly overestimates annihilation rates. Yet, this is probably a small contribution to the error in the computation of $Q_{\text{pair},\nu_i}^{(+)}$ in a moment scheme, and for this study at least, we approximate $\langle\omega_{(\nu_i)}\rangle_{\text{pair}}$ by the energy-weighted average energy (in the M1 scheme, converting from $\langle\epsilon\rangle$ to $\langle\omega_{(\nu_i)}\rangle_{\text{pair}}$ is done by assuming a thermal distribution of neutrinos).

The main issues with the computation of Eq. (21) in the two-moment formalism are that it relies on M1 estimates of the neutrino pressure tensor, and that it is significantly affected by the overdensity of polar neutrinos in the M1 scheme. To study these effects, we rewrite Eq. (21) as

$$Q_{\text{pair},\nu_i}^{(+)} = \frac{C_{\nu_i\bar{\nu}_i}^{\text{pair}} G_F^2}{3\pi\hbar^4 c^3} \langle\omega_{(\nu_i)}\rangle_{\text{pair}} \kappa_{(\nu_i)} E\bar{E}, \quad (24)$$

with $\kappa_{(\nu_i)}$ a dimensionless factor capturing the angular distribution of (anti)neutrinos. As $Q_{\text{pair},\nu_i}^{(+)} \propto E\bar{E}$, Fig. 11 provides us with an estimate of the impact on $Q_{\text{pair},\nu_i}^{(+)}$ of the M1 code's inaccurate values for the neutrino energy density. The M1 code would overestimate annihilation of

electron neutrinos by a factor of ~ 2 , and of heavy-lepton neutrinos by a factor of ~ 3 . The geometric factor κ has the opposite effect. In the M1 approximation, the assumed distribution function of polar neutrinos is more forward-peaked than what we find with the MC code. As a result, κ is significantly underestimated when using M1. This last effect is shown on Fig. 12: in most of the polar regions, κ is larger by factors of 3–5 in the MC code than in the M1 code, with peak ratios of ~ 100 . Accounting for both effects, we estimate that, given a good estimate of $\langle \omega(\nu_i) \rangle_{\text{pair}}$, the two-moment code captures the impact of pair annihilations within a factor of 2–3.

To help with future computations of the $\nu\bar{\nu}$ annihilation rate in two-moment simulations, we also provide direct measurements of the geometric factor κ in the MC code (Fig. 12). We note that, in the polar regions, κ is largely

independent of latitude, and mostly depends on the distance to the remnant. In Fig. 13, we show that κ is reasonably well fitted by the expression

$$\kappa(r) = \min(\kappa_0, Ae^{-r/W}) \quad (25)$$

with r the radius and, for electron neutrinos, $\kappa_0 = 0.53$, $W = 37$ km, while for heavy-lepton neutrinos, $\kappa_0 = 0.45$, $W = 43$ km. In theory, it may be interesting to use these fits in simulations performed with the M1 code. However, we should note that this will not get rid of errors caused by inaccurate neutrino energy densities in M1 simulations.

At the very least, we can use our results to estimate the accuracy of existing approximations used to compute the neutrino pair annihilation rate. For example, Fujibayashi *et al.* [38] use two different methods to compute that rate in

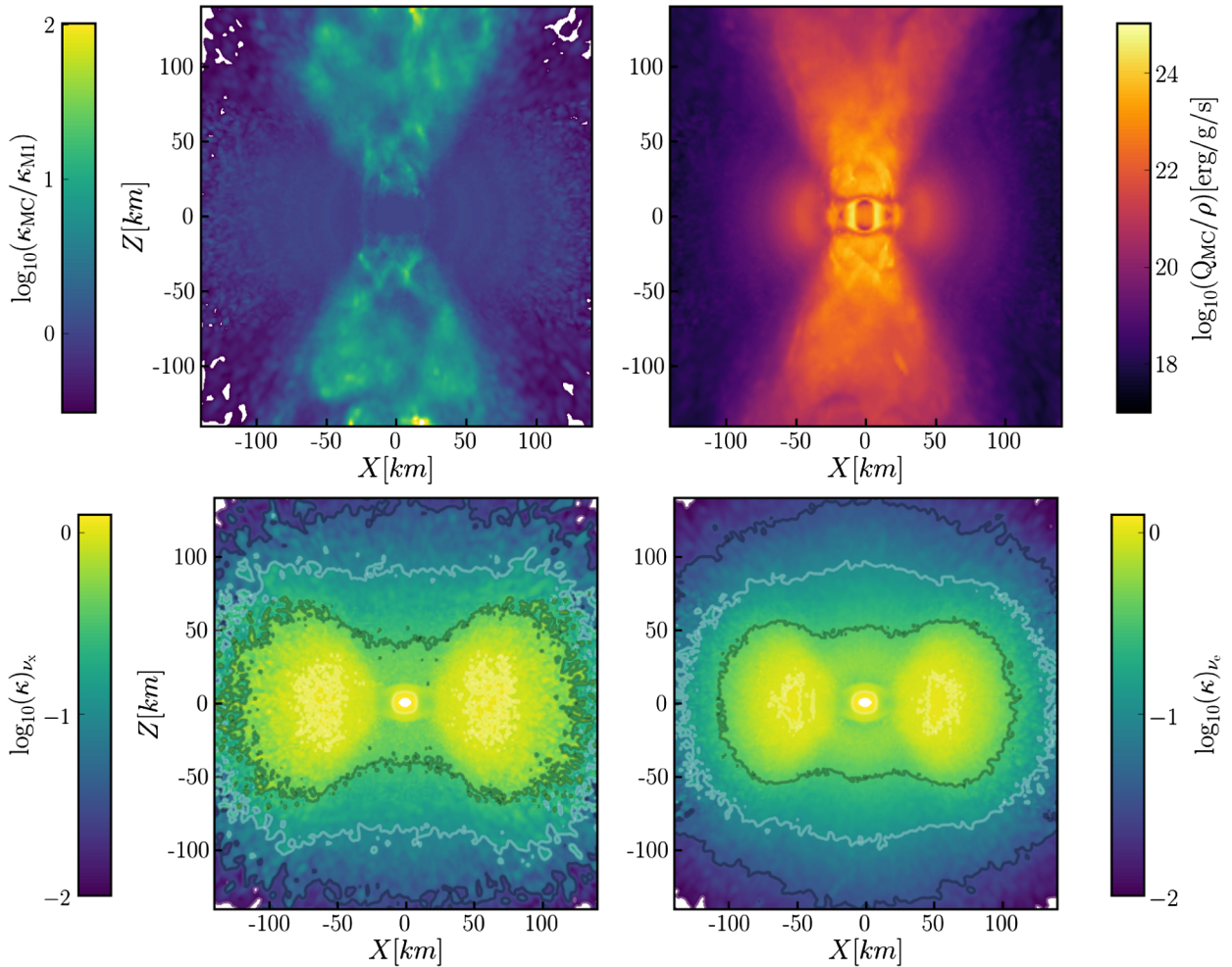


FIG. 12. Vertical slices through the merger remnant. Top: The specific energy deposition rate due to $\nu\bar{\nu}$ pair annihilation using the neutrino moments and average energy predicted by the MC code (right), and the ratio of the geometric factor κ obtained from the MC and M1 codes (left). The latter provides an estimate of the error due solely to the use of the Minerbo closure in the computation of Eq. (24). Bottom: The geometric factor κ in Eq. (24), for $\nu_x\bar{\nu}_x$ annihilation (left) and $\nu_e\bar{\nu}_e$ annihilation (right). Note that as the MC code only stores moments normalized to the energy density E (i.e., F^i/E , P_{ij}/E), the computation of Q_{MC} still uses the energy density evolved by the M1 code.

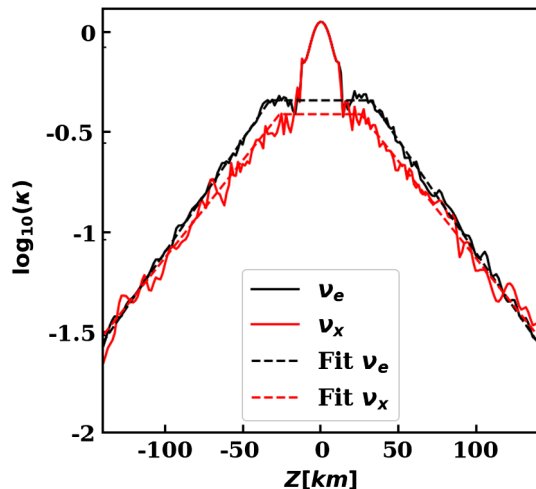


FIG. 13. Geometric factor κ in Eq. (24), along the polar axis. We show results for electron and heavy-lepton neutrinos, as well as best-fit curves using Eq. (25). The fits ignore the high-density regions inside the remnant neutron star, where pair annihilation is a subdominant process.

their simulations: one using the pressure provided by the Minerbo closure, and one assuming an isotropic distribution of neutrinos ($\kappa \sim 1.1$). Our results indicate that the second is a slightly more accurate approximation of κ than the first within 50 km of the remnant, where most of the pair annihilation energy is deposited. However, even there it is a factor of ~ 2 too high, and this error on κ acts in the same direction as the error due to the overestimated energy density at the poles. Once both sources of errors are taken into account, it appears that consistently using the Minerbo closure during all calculations is in fact more accurate.

Finally, we can provide an estimate of the heating rate due to pair annihilation in our simulation. In Fig. 12, we show the heating rate per unit mass. Fujibayashi *et al.* [38] estimate that the terminal Lorentz factor of the outflows is

$$\Gamma_f \sim 1.1 \frac{(Q/\rho)}{10^{24} \text{ erg/g/s}} \frac{\tau_{\text{heat}}}{1 \text{ ms}}, \quad (26)$$

with τ_{heat} the time during which the outflows are heated at a constant rate Q/ρ . The observed heating rate would make the polar outflows mildly relativistic, as observed in [38]. We can also look at the total energy deposition rate in the polar outflows, i.e., in regions with $\theta < 30^\circ$ and $\rho < 10^{10} \text{ g/cm}^3$ (the exact value is not very sensitive to changes of the limiting density, even by an order of magnitude). We find an energy deposition $Q_{\text{pair,tot}} \sim 3 \times 10^{50} \text{ erg/s}$. If we assume that the neutrino luminosity decreases on a time-scale of $\sim 50 \text{ ms}$, as in [38], we find a total energy deposition $\sim 1.5 \times 10^{49} \text{ erg}$, close to the kinetic energy of the polar ejecta measured in [38] ($\sim 10^{49} \text{ erg}$ in their simulation using the Minerbo closure to compute the annihilation rate). This qualitative agreement is not overly

surprising. Using our MC code, we have just argued that an M1 estimate of the annihilation rate should be correct within a factor of $\sim 2-3$. Pair annihilation is thus likely to play an important role in the dynamics of polar outflows. Whether this would really result in mildly relativistic outflows is not, however, obvious. Both our simulations and those in [38] neglect the impact of magnetic fields, and in particular of viscous heating driven by magnetic turbulence. Viscous radiation-hydrodynamics simulations in axisymmetry [39] find polar outflows energized by a combination of viscous heating and pair annihilation. Whether these outflows can be driven to mildly relativistic speeds will presumably depend on the unknown strength of the viscous heating and the baryon loading of the polar regions.

Overall, we find that multiple approximations made in the M1 scheme create errors of factors of a few in the computation of the $\nu\bar{\nu}$ annihilation rate. Yet, these errors partially cancel, and we find that a two-moment scheme using the Minerbo closure and informed by a reasonable estimate of the average neutrino energy can capture the neutrino pair annihilation rate within a factor of $\sim 2-3$. While probably insufficient for detailed studies of the impact of neutrino pair-annihilation on the dynamics of polar outflows, such accuracy is a much more favorable result for the two-moment scheme than one might have assumed before comparison with MC results.

V. CONCLUSIONS

We perform the first time-dependent, general relativistic, Monte Carlo radiation transport simulation of neutrinos in the remnant of a binary neutron star merger. The premerger system was a $1.2 M_\odot - 1.2 M_\odot$ system with the neutron star matter described using the LS220 equation of state. That system forms a massive neutron star—accretion disk remnant, with bright neutrino emission from both the disk and the hot neutron star. While we do not couple the MC evolution to the fluid evolution, we use our results to estimate important sources of errors in more approximate transport algorithms currently used in merger simulations. In particular, we focus on the limitations of the gray two-moment scheme with analytical Minerbo closure, as implemented in the SpEC code.

We find that the Minerbo closure providing us with an analytical estimate of the neutrino pressure tensor is very inaccurate in the low-density polar regions. These regions are of great importance for EM counterparts to neutron star mergers. It is there that the hot, high Y_e material powering optical kilonovae is most likely ejected. Neutrinos in polar regions are also likely to impact the production of short gamma-ray bursts. An important consequence of this inexact closure is that the energy density of neutrinos in the polar regions is strongly overestimated when using the M1 scheme, by $\sim 50\%$ for electron-type neutrinos and 100% for heavy-lepton neutrinos.

The average energy of the neutrinos, on the other hand, is relatively well approximated in the polar regions by two-moment schemes that evolve both the energy and number density of neutrinos (within $\sim 10\%$), but inexact closer to the equatorial plane. We also show that the energy spectrum of electron-type neutrinos is harder than the blackbody spectrum usually assumed in the gray M1 scheme.

Combining these various sources of errors, we can estimate that the absorption rates for charged-current reactions responsible for the evolution of the composition of the outflows may be off by factors of ~ 1.5 – 2 in M1 simulations, potentially a fairly significant limitation to our ability to model the composition of the outflows, and thus kilonovae. The practical impact of these errors in the M1 scheme on kilonova models remains, however, an open question. We already know that including neutrino absorption in simulations radically changes the composition of the outflows [33], while errors in the estimated neutrino energy leading to factor of a few changes in the absorption rate can modify the composition of the polar outflows by $\Delta Y_e \sim 0.05$ – 0.1 [44]. Considering our estimate of the error in the neutrino absorption rate obtained using our most up-to-date M1 scheme, it may be reasonable to assume that the change in Y_e due to the remaining approximations in the M1 scheme will be slightly smaller than the errors observed in [44]: important for accurate kilonova modeling, but not for our qualitative understanding of merger outflows. Considering that neutron star mergers are complex non-linear systems, however, this cannot be rigorously demonstrated at this point. A more accurate statement will have to wait for simulations with a full coupling of the MC scheme (or another improved neutrino transport method) to the fluid evolution.

We also consider the impact of the M1 approximation on estimates of the $\nu\bar{\nu} \rightarrow e^+e^-$ annihilation rate. While two different issues in M1 simulations each induce errors of factors $\gtrsim 2$, these errors partially cancel. An M1 scheme with a good estimate of the average energy of the neutrinos is likely capable of predicting the neutrino annihilation rate within factors of 2–3. While certainly significant, these errors are smaller than one might have guessed prior to this study. Including pair-annihilation effects within a two-moment scheme probably leads to at least qualitatively correct behavior of the polar outflows.

Another important objective of this simulation is to assess the feasibility of using time-averaged moments computed from a low-resolution MC evolution as closure for the two-moment scheme, thus removing the need to use the approximate Minerbo closure or to assume a given energy spectrum [41]. We find that the time dependence of the neutrino distribution function over the orbital timescale

of the remnant is relatively weak, partially justifying the use of moments averaged over timescales comparable to the dynamical timescale of the system. Additionally, our choice to avoid performing MC evolutions in high-optical depth regions (where $\kappa\Delta x \gtrsim 1$) and to instead simply provide boundary conditions approximating a thermal distribution of neutrinos in these regions does not appear to create significant errors, at least when compared with a simulation placing that boundary deeper in the remnant ($\kappa\Delta x \gtrsim 10$).

We thus estimate that we can provide moments of the neutrino distribution function with statistical noise at the level of a few percent with as little as $\sim 2.5 \times 10^7$ MC packets (for a simulation with 2.8×10^7 finite volume cells). This indicates that the two-moment scheme with MC closure that we recently proposed [41] is computationally affordable in simulations of postmerger remnants, and if stable may provide a convenient way to improve upon the standard two-moment algorithm with Minerbo closure. At the current accuracy of the MC scheme, and considering current errors in the M1 scheme of up to a factor of 2 in the local energy density and expected neutrino absorption rate, and $\sim 10\%$ – 20% in the average energy of the neutrinos, such a coupled algorithm could, in principle, reduce relative errors in the two-moment scheme by an order of magnitude.

ACKNOWLEDGMENTS

The authors thank the members of the SXS Collaboration for helpful discussions over the course of this project. F.F. acknowledges support from NASA through Grant No. 80NSSC18K0565. M. D. acknowledges support through NSF Grant No. PHY-1402916. H. P. gratefully acknowledges support from the NSERC Canada, the Canada Research Chairs Program and the Canadian Institute for Advanced Research. L. K. acknowledges support from NSF Grant No. PHY-1606654, and M. S. from NSF Grants No. PHY-1708212, No. PHY-1708213, and No. PHY-1404569. L. K. and M. S. also thank the Sherman Fairchild Foundation for their support. Computations were performed on the supercomputer Briarée from the Université de Montréal, managed by Calcul Québec and Compute Canada. The operation of these supercomputers is funded by the Canada Foundation for Innovation (CFI), NanoQuébec, RMGA and the Fonds de recherche du Québec—Nature et Technologie (FRQ-NT). Computations were also performed on the Zwicky and Wheeler clusters at Caltech, supported by the Sherman Fairchild Foundation and by NSF Award No. PHY-0960291.

- [1] B. P. Abbott *et al.* (Virgo and LIGO Scientific), *Phys. Rev. Lett.* **119**, 161101 (2017).
- [2] B. P. Abbott, R. Abbott, T. D. Abbott, F. Acernese, K. Ackley, C. Adams, T. Adams, P. Addesso, R. X. Adhikari, V. B. Adya *et al.*, *Appl. J. Lett.* **848**, L12 (2017).
- [3] M. M. Kasliwal *et al.*, *Science* **358**, 1559 (2017).
- [4] D. A. Coulter, R. J. Foley, C. D. Kilpatrick, M. R. Drout, A. L. Piro, B. J. Shappee, M. R. Siebert, J. D. Simon, N. Ulloa, D. Kasen, B. F. Madore, A. Murguia-Berthier, Y. C. Pan, J. X. Prochaska, E. Ramirez-Ruiz, A. Rest, and C. Rojas-Bravo, *Science* **358**, 1556 (2017).
- [5] R. Chornock *et al.*, *Astrophys. J. Lett.* **848**, L19 (2017).
- [6] P. S. Cowperthwaite *et al.*, *Astrophys. J. Lett.* **848**, L17 (2017).
- [7] D. Kasen, B. Metzger, J. Barnes, E. Quataert, and E. Ramirez-Ruiz, *Nature* **551**, 80 (2017).
- [8] C. D. Kilpatrick, R. J. Foley, D. Kasen, A. Murguia-Berthier, E. Ramirez-Ruiz, D. A. Coulter, M. R. Drout, A. L. Piro, B. J. Shappee, K. Boutsia, C. Contreras, F. Di Mille, B. F. Madore, N. Morrell, Y. C. Pan, J. X. Prochaska, A. Rest, C. Rojas-Bravo, M. R. Siebert, J. D. Simon *et al.*, *Science* **358**, 1583 (2017).
- [9] C. McCully, D. Hiramatsu, D. A. Howell, G. Hosseinzadeh, I. Arcavi, D. Kasen, J. Barnes, M. M. Shara, T. B. Williams, P. Väisänen, S. B. Potter, E. Romero-Colmenero, S. M. Crawford, D. A. H. Buckley, J. Cooke, I. Andreoni, T. A. Pritchard, J. Mao, M. Gromadzki, and J. Burke, *Astrophys. J. Lett.* **848**, L32 (2017).
- [10] M. Nicholl *et al.*, *Astrophys. J. Lett.* **848**, L18 (2017).
- [11] E. Pian *et al.*, *Nature* **551**, 67 (2017).
- [12] S. J. Smartt *et al.*, *Nature* **551**, 75 (2017).
- [13] M. Soares-Santos *et al.* (Dark Energy Survey and Dark Energy Camera GW-EM Collaboration), *Astrophys. J. Lett.* **848**, L16 (2017).
- [14] N. R. Tanvir *et al.*, *Astrophys. J. Lett.* **848**, L27 (2017).
- [15] P. A. Evans *et al.*, *Science* **358**, 1565 (2017).
- [16] J. M. Lattimer and D. N. Schramm, *Astrophys. J.* **210**, 549 (1976).
- [17] L. X. Li and B. Paczynski, *Astrophys. J.* **507**, L59 (1998).
- [18] L. F. Roberts, D. Kasen, W. H. Lee, and E. Ramirez-Ruiz, *Astrophys. J. Lett.* **736**, L21 (2011).
- [19] D. Kasen, N. R. Badnell, and J. Barnes, *Astrophys. J.* **774**, 25 (2013).
- [20] M. Tanaka and K. Hotokezaka, *Astrophys. J.* **775**, 113 (2013).
- [21] R. Fernández, E. Quataert, J. Schwab, D. Kasen, and S. Rosswog, *Mon. Not. R. Astron. Soc.* **449**, 390 (2015).
- [22] O. Just, A. Bauswein, R. A. Pulpillo, S. Goriely, and H. T. Janka, *Mon. Not. R. Astron. Soc.* **448**, 541 (2015).
- [23] R. Fernández, F. Foucart, D. Kasen, J. Lippuner, D. Desai, and L. F. Roberts, *Classical Quantum Gravity* **34**, 154001 (2017).
- [24] K. Kiuchi, Y. Sekiguchi, K. Kyutoku, M. Shibata, K. Taniguchi, and T. Wada, *Phys. Rev. D* **92**, 064034 (2015).
- [25] L. Lehner, S. L. Liebling, C. Palenzuela, O. L. Caballero, E. O'Connor, M. Anderson, and D. Neilsen, *Classical Quantum Gravity* **33**, 184002 (2016).
- [26] D. M. Siegel and B. D. Metzger, *Phys. Rev. Lett.* **119**, 231102 (2017).
- [27] B. Giacomazzo, J. Zrake, P. C. Duffell, A. I. MacFadyen, and R. Perna, *Astrophys. J.* **809**, 39 (2015).
- [28] M. Shibata and K. Kiuchi, *Phys. Rev. D* **95**, 123003 (2017).
- [29] D. Radice, *Astrophys. J. Lett.* **838**, L2 (2017).
- [30] L. Baiotti and L. Rezzolla, *Rep. Prog. Phys.* **80**, 096901 (2017).
- [31] V. Paschalidis, *Classical Quantum Gravity* **34**, 084002 (2017).
- [32] R. Surman, G. C. McLaughlin, M. Ruffert, H. T. Janka, and W. R. Hix, *Astrophys. J. Lett.* **679**, L117 (2008).
- [33] S. Wanajo, Y. Sekiguchi, N. Nishimura, K. Kiuchi, K. Kyutoku, and M. Shibata, *Astrophys. J. Lett.* **789**, L39 (2014).
- [34] L. Dessart, C. D. Ott, A. Burrows, S. Rosswog, and E. Livne, *Astrophys. J.* **690**, 1681 (2009).
- [35] J. D. Salmonson and J. R. Wilson, *Astrophys. J.* **517**, 859 (1999).
- [36] R. Birkel, M. A. Aloy, H. T. Janka, and E. Müller, *Astron. Astrophys.* **463**, 51 (2007).
- [37] O. Just, M. Obergaulinger, H. T. Janka, A. Bauswein, and N. Schwarz, *Astrophys. J. Lett.* **816**, L30 (2016).
- [38] S. Fujibayashi, Y. Sekiguchi, K. Kiuchi, and M. Shibata, *Astrophys. J.* **846**, 114 (2017).
- [39] S. Fujibayashi, K. Kiuchi, N. Nishimura, Y. Sekiguchi, and M. Shibata, *Astrophys. J.* **860**, 64 (2018).
- [40] A. Perego, H. Yasin, and A. Arcones, *J. Phys. G* **44**, 084007 (2017).
- [41] F. Foucart, *Mon. Not. R. Astron. Soc.* **475**, 4186 (2018).
- [42] F. Foucart, R. Haas, M. D. Duez, E. O'Connor, C. D. Ott, L. Roberts, L. E. Kidder, J. Lippuner, H. P. Pfeiffer, and M. A. Scheel, *Phys. Rev. D* **93**, 044019 (2016).
- [43] F. Foucart, E. O'Connor, L. Roberts, M. D. Duez, R. Haas, L. E. Kidder, C. D. Ott, H. P. Pfeiffer, M. A. Scheel, and B. Szilagy, *Phys. Rev. D* **91**, 124021 (2015).
- [44] F. Foucart, E. O'Connor, L. Roberts, L. E. Kidder, H. P. Pfeiffer, and M. A. Scheel, *Phys. Rev. D* **94**, 123016 (2016).
- [45] G. N. Minerbo, *J. Quant. Spectrosc. Radiat. Transfer* **20**, 541 (1978).
- [46] A. Malkus, J. P. Kneller, G. C. McLaughlin, and R. Surman, *Phys. Rev. D* **86**, 085015 (2012).
- [47] A. Malkus, G. C. McLaughlin, and R. Surman, *Phys. Rev. D* **93**, 045021 (2016).
- [48] W. R. Wu, H. Duan, and Y. Z. Qian, *Phys. Lett. B* **752**, 89 (2016).
- [49] Y. L. Zhu, A. Perego, and G. C. McLaughlin, *Phys. Rev. D* **94**, 105006 (2016).
- [50] See <http://www.black-holes.org/SpEC.html>.
- [51] L. Lindblom, M. A. Scheel, L. E. Kidder, R. Owen, and O. Rinne, *Classical Quantum Gravity* **23**, S447 (2006).
- [52] M. D. Duez, F. Foucart, L. E. Kidder, H. P. Pfeiffer, M. A. Scheel, and S. A. Teukolsky, *Phys. Rev. D* **78**, 104015 (2008).
- [53] F. Foucart, M. B. Deaton, M. D. Duez, L. E. Kidder, I. MacDonald, C. D. Ott, H. P. Pfeiffer, M. A. Scheel, B. Szilagy, and S. A. Teukolsky, *Phys. Rev. D* **87**, 084006 (2013).
- [54] K. S. Thorne, *Mon. Not. R. Astron. Soc.* **194**, 439 (1981).
- [55] M. Shibata, K. Kiuchi, Y. Sekiguchi, and Y. Suwa, *Prog. Theor. Phys.* **125**, 1255 (2011).

- [56] R. Bollig, H. T. Janka, A. Lohs, G. Martínez-Pinedo, C. J. Horowitz, and T. Melson, *Phys. Rev. Lett.* **119**, 242702 (2017).
- [57] S. Rosswog and M. Liebendörfer, *Mon. Not. R. Astron. Soc.* **342**, 673 (2003).
- [58] A. Burrows, S. Reddy, and T. A. Thompson, *Nucl. Phys.* **A777**, 356 (2006).
- [59] S. Richers, D. Kasen, E. O'Connor, R. Fernandez, and C. D. Ott, *Astrophys. J.* **813**, 38 (2015).
- [60] B. R. Ryan, J. C. Dolence, and C. F. Gammie, *Astrophys. J.* **807**, 31 (2015).
- [61] E. O'Connor, *Astrophys. J. Suppl. Ser.* **219**, 24 (2015).
- [62] J. M. Smit, J. Cernohorsky, and C. P. Dullemond, *Astron. Astrophys.* **325**, 203 (1997).
- [63] J. M. Lattimer and F. D. Swesty, *Nucl. Phys.* **A535**, 331 (1991).
- [64] E. O'Connor and C. D. Ott, *Classical Quantum Gravity* **27**, 114103 (2010).
- [65] K. Kiuchi, P. Cerdá-Durán, K. Kyutoku, Y. Sekiguchi, and M. Shibata, *Phys. Rev. D* **92**, 124034 (2015).